Preprint: Under Review 1–27

ProtoECGNet: Case-Based Interpretable Deep Learning for Multi-Label ECG Classification with Contrastive Learning

Sahil Sethi[1,2] SETHIS@UCHICAGO.EDU
David Chen[2] CHEND5@UCHICAGO.EDU
Thomas Statchen[1,2] TSTATCHEN@UCHICAGO.EDU
Michael C. Burkhart[2] BURKH4RT@UCHICAGO.EDU
Nipun Bhandari[3] NIBHANDARI@UCDAVIS.EDU
Bashar Ramadan[4,*] BASHAR.RAMADAN@BSD.UCHICAGO.EDU
Brett Beaulieu-Jones[2,*] BEAULIEUJONES@UCHICAGO.EDU

[1] *Pritzker School of Medicine, University of Chicago, IL, USA*
[2] *Center for Computational Medicine & Clinical AI, Section of Biomedical Data Science, Department of Medicine, University of Chicago, IL, USA*
[3] *Division of Cardiovascular Medicine, Department of Internal Medicine, University of California Davis, CA, USA*
[4] *Section of Hospital Medicine, Department of Medicine, University of Chicago, IL, USA*

**These authors contributed equally*

Abstract

Deep learning-based electrocardiogram (ECG) classification has shown impressive performance but clinical adoption has been slowed by the lack of transparent and faithful explanations. Post hoc methods such as saliency maps may fail to reflect a model's true decision process. Prototype-based reasoning offers a more transparent alternative by grounding decisions in similarity to learned representations of real ECG segments—enabling faithful, case-based explanations. We introduce ProtoECGNet, a prototype-based deep learning model for interpretable, multi-label ECG classification. ProtoECGNet employs a structured, multi-branch architecture that reflects clinical interpretation workflows: it integrates a 1D CNN with global prototypes for rhythm classification, a 2D CNN with time-localized prototypes for morphology-based reasoning, and a 2D CNN with global prototypes for diffuse abnormalities. Each branch is trained with a prototype loss designed for multi-label learning, combining clustering, separation, diversity, and a novel contrastive loss that encourages appropriate separation between prototypes of unrelated classes while allowing clustering for frequently co-occurring diagnoses. We evaluate ProtoECGNet on all 71 diagnostic labels from the PTB-XL dataset, demonstrating competitive performance relative to state-of-the-art black-box models while providing structured, case-based explanations. To assess prototype quality, we conduct a structured clinician review of the final model's projected prototypes, finding that they are rated as representative and clear. ProtoECGNet shows that prototype learning can be effectively scaled to complex, multi-label time-series classification, offering a practical path toward transparent and trustworthy deep learning models for clinical decision support.

1. Introduction

Deep learning (DL) has achieved strong performance across a wide range of diagnostic and predictive tasks in medicine. (Aggarwal et al., 2021; Petmezas et al., 2022; Khera et al., 2024; Oliveira et al., 2023; Barnes et al., 2023; Sethi et al., 2025; Sun et al., 2021). In cardiology, DL-based electrocardiogram (ECG) interpretation is of great interest because ECGs are central to diagnosing many diseases like arrhythmias, myocardial infarction, and structural heart disease (Carrington et al., 2022; Birnbaum et al., 2014). DL models have demonstrated strong, and in some cases, cardiologist-level performance in ECG classification (Hannun et al., 2019; Elias et al., 2022; He et al., 2023; Ouyang et al., 2024; Trivedi et al., 2025; Yuan et al., 2023), but their clinical deployment would be accelerated with increased transparency and trustworthiness in model predictions (Goettling et al., 2024). An example of a blackbox prediction for an ECG with an anteroseptal myocardial infarction (ASMI) is shown in Figure 1A.

Post hoc explainability methods—such as saliency maps and attention-based visualizations—are commonly used to interpret black-box deep learning models (Rudin, 2019; Adebayo et al., 2020). However, these methods generate outputs that are not necessarily aligned with the model's decision process. Prior studies have shown that saliency maps can be unstable, non-reproducible, and misaligned with human reasoning, particularly in medical domains (Adebayo et al., 2020; Alvarez-Melis and Jaakkola, 2018; Turbé et al., 2023). Most importantly, simply highlighting the parts of an ECG the model focused on is not the same as explaining why it made a specific diagnosis—as illustrated in Figure 1B. These limitations have led to growing interest in self-explaining models, where interpretability is embedded directly into the model architecture (Rudin, 2019; Tonekaboni et al., 2019).

Prototype-based models classify inputs by comparing them to a small set of learned, class-associated vectors called *prototypes*, each of which represents a localized region in the model's latent space. During inference, predictions are based on the similarity between an input and these prototypes—effectively grounding decisions in similarity to learned representative examples from the training set. This allows the model to produce case-based explanations that are inherently faithful to its internal decision process (see Figure 1C). Unlike saliency methods, prototype networks explicitly learn and are forced to use interpretable exemplars as part of their classification pipeline. However, existing prototype-based models for ECG interpretation have been limited in scope. Prior work has focused primarily on single-label rhythm classification tasks and used only single- or dual-lead signals (Ming et al., 2019; Xie et al., 2024). These approaches do not address the complexity of large-scale, multi-label ECG classification, where numerous cardiac abnormalities frequently co-occur and require diverse forms of temporal and spatial reasoning.

In this work, we introduce **ProtoECGNet**, a prototype-based deep learning architecture for interpretable, multi-label ECG classification. ProtoECGNet is designed to mirror the reasoning processes used by clinicians during ECG interpretation, combining multiple prototype types aligned with temporal and spatial diagnostic patterns. Our approach enables structured, case-based explanations without sacrificing predictive performance, even in large-scale, multi-label classification tasks. Our key contributions include:

1. **A customized prototype loss for multi-label ECG classification.** We build upon prior prototype learning objectives (Barnett et al., 2024; Wang et al., 2021),

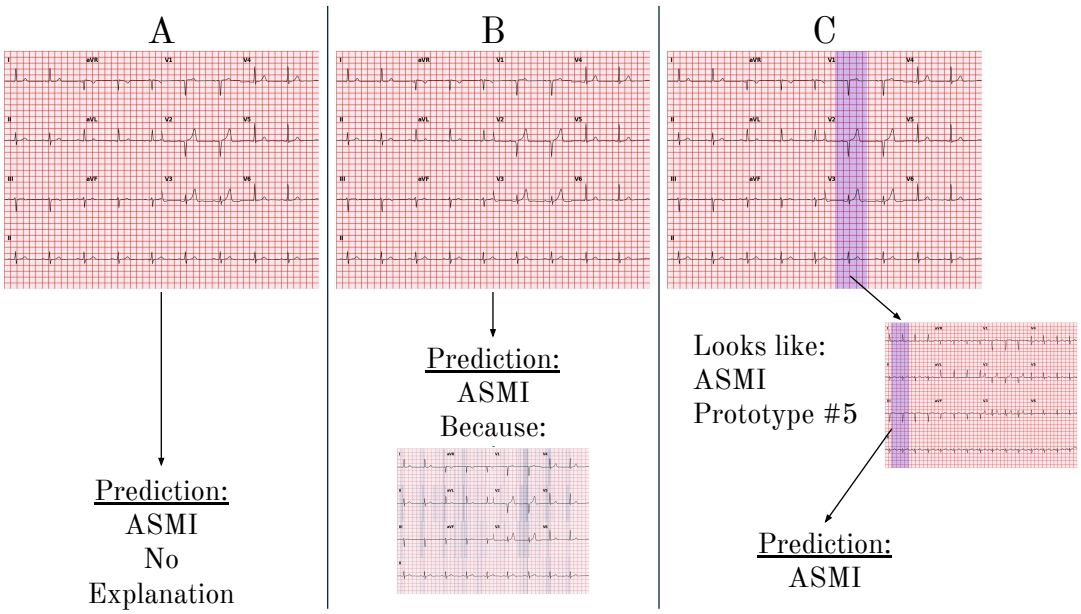

Figure 1: Illustration of interpretability approaches for ECG classification. **(A)** Black-box models such as convolutional neural networks (CNNs) can achieve strong performance on diagnostic tasks, but provide no inherent explanation for their predictions. **(B)** Post hoc explainability methods, such as saliency maps, attempt to highlight input regions deemed important by the model after a prediction is made. However, these visualizations are not part of the model's decision process and often fail to provide a meaningful explanation—simply indicating "where" the model looked does not explain "why" it made a decision. **(C)** Prototype-based models offer a self-explaining alternative: predictions are made by comparing a test input to a set of learned prototype vectors, each anchored to a real ECG segment. This enables case-based explanations that reflect the model's actual classification logic. ASMI = anteroseptal myocardial infarction.

modifying the loss formulation to better accommodate multi-label supervision. Specifically, we retain and adapt the clustering and separation terms to account for label co-occurrence, and introduce a novel *contrastive loss* designed for the multi-label prototype setting. Our contrastive loss encourages separation between prototypes assigned to rarely co-occurring diagnoses, while allowing prototypes for frequently co-occurring conditions to remain close in the latent space. This formulation structures the prototype geometry to reflect empirical co-occurrence patterns observed in the training data (e.g., Q-waves are a common co-occurrence across different forms of myocardial infarction) and improves classification performance.

2. **A multi-branch model architecture aligned with clinical reasoning.** ProtoECGNet consists of three specialized prototype branches: (1) a *1D rhythm model* with global prototypes designed to capture long-range temporal patterns, (2) a *2D*

morphology model with time-localized prototypes that leverage inter-lead spatial structure to identify focal waveform abnormalities, and (3) a *2D global model* with full-duration, full-lead prototypes for detecting diffuse or distributed ECG abnormalities. Each branch is trained independently on a disjoint subset of diagnostic labels, and their outputs are either aggregated via macro-averaging or fused using a learned classifier trained to predict all 71 labels in the PTB-XL dataset.

3. **Empirical evaluation of prototype quality by clinicians.** To assess the interpretability of the learned prototypes, we conducted a structured review in which two physicians independently rate all projected prototypes from the final model on multiple quality criteria, including clarity and class representativeness. This evaluation provides initial evidence that the model's explanations align with clinical expectations.

Generalizable Insights about Machine Learning in the Context of Healthcare

We show that prototype-based interpretability depends on how prototypes are defined, trained, and aligned with clinical reasoning. By organizing diagnostic labels into rhythm, morphology, and global categories, and assigning each to a dedicated prototype branch, ProtoECGNet reflects the structure of expert ECG interpretation and enables more domain-tailored explanations. Further, we demonstrate that prototype learning can be extended to multi-label tasks through careful loss design: our contrastive formulation allows the model to preserve meaningful overlap between co-occurring diagnoses while maintaining discriminative structure in the latent space. Unlike prior prototype models limited to narrow single-label classification tasks, our approach supports full-spectrum ECG interpretation across 71 diagnostic labels, producing real ECG segment–based explanations without relying on post hoc methods. This shows that interpretable models can scale to realistic clinical tasks when their architecture and objectives are designed with domain constraints in mind.

2. Related Work

2.1. Prototype-Based Learning

Prototype-based learning has emerged as a promising framework for interpretable machine learning, particularly following the introduction of ProtoPNet (Chen et al., 2019). Subsequent work has extended this paradigm in various directions: ProtoTree (Hase et al., 2019) structured prototypes hierarchically; TesNet (Wang et al., 2021) mapped prototypes to a hyperspherical latent space; ProtoPool (Rymarczyk et al., 2022) enabled soft sharing of prototypes across classes; and ProtoConcepts (Ma et al., 2023) combined prototypes with concept-based reasoning. These models have demonstrated interpretability benefits in imaging tasks, including breast cancer classification (Barnett et al., 2021), brain tumor detection (Wei et al., 2023), and chest X-ray analysis (Kim et al., 2021). However, most of this literature assumes mutually exclusive class labels and focuses on static 2-D images, limiting direct applicability to sequential medical data.

Prototype learning for time-series data remains underexplored. One adaptation to EEG classification uses a 2D CNN-based prototype model, treating multichannel signals as images and validating interpretability through a structured clinician study (Barnett et al., 2024). However, this approach used only global prototypes and addressed a single-label,

multi-class classification task. Existing prototype-based ECG models, such as ProSeNet (Ming et al., 2019) and PahNet (Xie et al., 2024), focus narrowly on rhythm detection using single- or dual-lead inputs, and neither supports multi-label classification. Moreover, PahNet does not include a prototype projection mechanism, preventing alignment between learned prototypes and real ECG segments—limiting its explanatory usefulness in clinical settings.

The most closely related work is xECGArch (Goettling et al., 2024), which introduces a dual-CNN model to separately capture short-term (morphological) and long-term (rhythmic) patterns in ECGs. However, xECGArch does not project prototypes onto real ECG segments and instead relies on post hoc saliency maps for interpretation, limiting its ability to provide case-based explanations. It is also restricted to binary atrial fibrillation detection using single-lead inputs. In contrast, ProtoECGNet is explicitly designed for multi-label, 12-lead ECG interpretation. It includes three clinically inspired prototype branches tailored to rhythm, morphology, and global abnormalities, with each prototype anchored to a real training segment for faithful explanation. The latent space is further structured using a custom contrastive loss that reflects real-world label co-occurrence. Our work extends prototype learning to a more complex and clinically realistic setting.

2.2. Contrastive Learning

While prototype learning offers an inherently interpretable model structure, it does not ensure that the learned prototypes reflect meaningful diagnostic variation—particularly in multi-label settings, where some conditions routinely co-occur. To address this, we introduce a contrastive loss tailored to multi-label prototype learning, designed to shape the prototype similarity space in alignment with label relationships observed in the training data.

Our approach is inspired by supervised contrastive learning, which has been widely used to structure encoder representations. SupCon (Khosla et al., 2021) and SimCLR (Chen et al., 2020) promote similarity among positive pairs and dissimilarity among negatives using log-softmax objectives over large batches. Multi-label extensions, such as MulSupCon (Zhang and Wu, 2024), weight similarity based on label overlap. However, these instance-level methods are not applicable to our setting, where the goal is to organize a fixed set of prototype vectors with known class assignments—not to embed unlabeled instances.

More relevant is the Joint Supervised Contrastive Loss (JSCL) proposed by Lin et al. (2023), which introduces a contrastive loss for multi-label classification by encouraging proximity between latent representations of examples with shared labels and pushing apart those with disjoint labels. JSCL operates on input embeddings and uses a log-ratio formulation. We adapt this idea for the prototype learning setting in two key ways. First, we apply the loss directly to the prototype vectors in the latent space, leveraging their fixed prototype-to-class assignments to define positive and negative pairs. Second, we replace the log-ratio formulation with a mean-difference objective: the average similarity between prototype pairs assigned to overlapping labels is contrasted against the average similarity of those with disjoint label sets. This formulation is well-suited to our structured prototype setting and encourages the latent space to reflect realistic co-occurrence patterns.

3. Methods

3.1. Dataset and Label Grouping

We used the PTB-XL dataset, a publicly available collection of 21,799 10-second, 12-lead ECGs from 18,869 patients sampled at both 500 Hz and 100 Hz (Wagner et al., 2020). Each ECG was annotated with one or more of 71 SCP-ECG diagnostic labels spanning arrhythmias, conduction disorders, infarction patterns, and morphological abnormalities. We retained the original dataset split from Wagner et al. (2020)—using folds 1-8 for training and fold 9 for validation. We reported performance metrics on fold 10, using it as a hold-out test set. To align with the dataset's benchmarks, the term-centric macro AUROC from Strodthoff et al. (2021) was chosen as the primary performance metric. Appendix D details how ECGs were visualized for figures and prototype review.

The dataset contains several label groupings (e.g., diagnostic superclasses), but these were unsuitable for our desired training process. Consequently, two physicians—one board-certified in cardiology and the other in internal medicine—grouped the 71 labels into three clinically meaningful prototype categories based on the type of visual reasoning required for diagnosis: **(1) rhythm-based diagnoses**—require temporal pattern analysis across full-length ECG signals, often discernible from a single lead; **(2) morphology-based diagnoses**—require localized waveform shape or inter-lead comparisons over short time intervals; **(3) global diagnoses**—require full-lead patterns spanning the full ECG duration. In total, 16 diagnoses were grouped into the 1D rhythm branch, 52 into the 2D morphology branch, and 3 into the 2D global branch. These groupings are detailed in Appendix G.

3.2. Preprocessing

As the lower end of the frequency range for a normal ECG is 0.5 Hz (Zheng et al., 2020), we applied a first-order Butterworth high-pass filter with a 0.5 Hz cutoff. No low-pass filter was applied, as we used the 100 Hz samples from the dataset.

3.3. Model Architecture

ProtoECGNet consisted of three independent prototype-based branches, each specialized for a distinct type of ECG diagnostic reasoning: rhythm-based, morphology-based, and global abnormalities (see Figure 2 and Figure 5). Each branch processed the same raw 12-lead ECG input of shape (12×1000) but applied a different label subset.

1D Rhythm Branch. This branch was designed to capture long-range temporal dependencies characteristic of rhythm abnormalities. We adopted the ResNet1D-18 architecture from Strodthoff et al. (2021), operating on input ECGs of shape (12×1000). The architecture consisted of an initial strided convolution, followed by four residual blocks with increasing channel depth. Feature maps were pooled with an adaptive average pooling layer to produce fixed-length latent representations per lead. These representations formed the prototype matching space for the 1D rhythm model.

2D Morphology Branch. To detect localized waveform abnormalities that depend on spatial relationships across ECG leads—such as ST elevation or pathological Q waves—we used a 2D convolutional neural network that treats the 12-lead ECG as a spatial-temporal

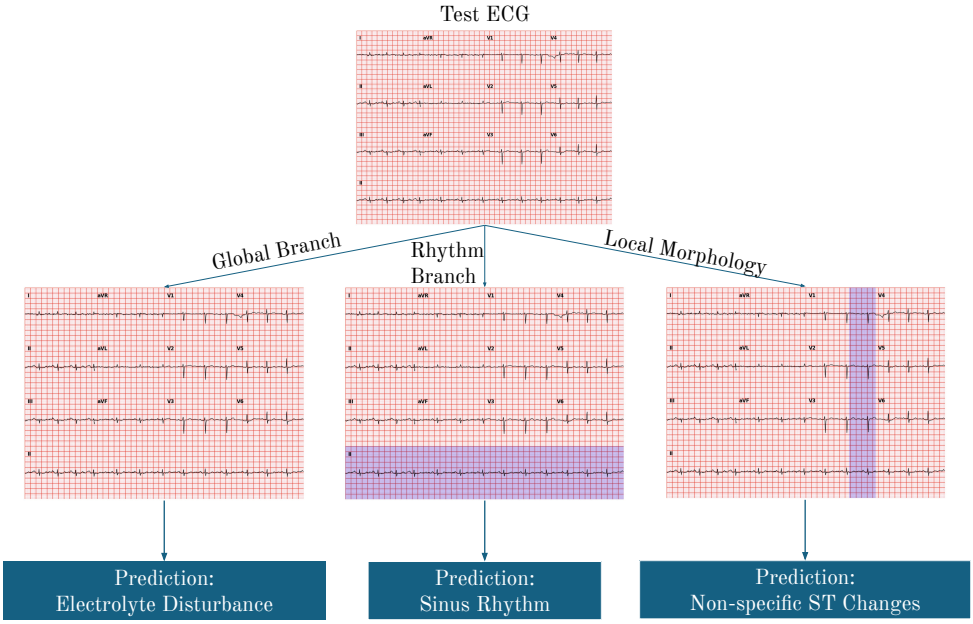

Figure 2: Multi-branch approach. See Figure 5 for detailed architectural information.

matrix. Input ECGs are shaped as $(1\times12\times1000)$, where the vertical dimension corresponded to the 12 leads and the horizontal dimension to time. The model used a modified ResNet18 (He et al., 2015) backbone in which the first convolutional layer was adapted to accept single-channel 2D inputs with a filter size of (12×7). Pretrained ImageNet weights were loaded for the remaining layers. To preserve temporal resolution, the global average pooling layer was removed, resulting in a final feature map of shape $(512 \times 1 \times 32)$, where the temporal axis was down sampled from 1000 to 32 steps. This branch used *partial prototypes* that spanned a small temporal window (3 units, approximately 0.94 seconds at 100 Hz) and were applied in a sliding fashion across the latent time dimension. During inference, the model computed similarity scores between each partial prototype and all possible time-localized windows of the test ECG's latent feature map. Top-k pooling was then applied to aggregate the k most activated positions into a final similarity score per prototype.

2D Global Branch. Diagnoses that required global ECG interpretation—such as electrolyte disturbances—were handled using the same 2D CNN architecture as the 2D morphology branch. Inputs had shape $(1\times12\times1000)$ and yielded latent maps of shape $(512\times1\times32)$. However, this branch used *global prototypes* spanning all leads and the full time axis.

Prototype Layer. All prototype matching occurred in the latent feature space of the CNN feature extractor backbones. Each branch contained its own prototype layer with P learnable prototypes assigned to specific class labels. Let $z_i \in \mathbb{R}^D$ be a patch from the latent feature map and $p_j \in \mathbb{R}^D$ a prototype. We defined the similarity between them as:

$$\mathrm{S}(z_i, p_j) = \left\langle \frac{a \cdot z_i}{\|z_i\|_2}, \frac{p_j}{\|p_j\|_2} \right\rangle \tag{1}$$

where $\langle \cdot, \cdot \rangle$ denotes the dot product and the scaling factor a adjusts the magnitude of the similarity score based on the latent dimensionality. This cosine similarity variant, adapted from Barnett et al. (2024), was used to compute similarity between each prototype and regions of the latent feature map. For *partial prototypes* (used in the morphology branch), each prototype slid across the temporal axis of the latent feature map and produced a similarity score at each time step. We then applied top-k pooling across these scores to retain the k highest activations, and computed their average to obtain a single similarity score per prototype per input. For *global prototypes* (used in the rhythm and 2D global branches), each prototype spanned the entire temporal dimension of the latent space, yielding a single similarity score per input without the need for pooling.

3.4. Prototype Loss Function

Each branch was trained using a composite loss function:

$$\mathcal{L}_{\text{total}} = \mathcal{L}_{\text{BCE}} + \lambda_{\text{clst}} \cdot \mathcal{L}_{\text{clst}} + \lambda_{\text{sep}} \cdot \mathcal{L}_{\text{sep}} + \lambda_{\text{div}} \cdot \mathcal{L}_{\text{div}} + \lambda_{\text{cntrst}} \cdot \mathcal{L}_{\text{cntrst}} \tag{2}$$

where each λ is a tunable hyperparameter controlling the strength of its loss component.

Binary Cross-Entropy Loss.

$$\mathcal{L}_{\text{BCE}} = -\frac{1}{N} \sum_{i=1}^{N} \sum_{j=1}^{C} w_j \left[y_{ij} \log \sigma(z_{ij}) + (1 - y_{ij}) \log(1 - \sigma(z_{ij})) \right] \tag{3}$$

This loss penalized incorrect predictions for each class independently in a multi-label setting. Here, $y_{ij} \in \{0, 1\}$ is the ground truth label for sample i and class j; z_{ij} is the predicted logit; $\sigma(\cdot)$ is the sigmoid function; and w_j is a class weight.

Clustering Loss.

$$\mathcal{L}_{\text{clst}} = -\frac{1}{N} \sum_{i=1}^{N} \max_{p \in \mathcal{P}_i^+} S_{ip} \tag{4}$$

This term encouraged each prototype to have high similarity to at least one input that shared its assigned class label. S_{ip} is the similarity between input i and prototype p, and $\mathcal{P}_i^+$ denotes the set of prototypes assigned to any of the labels present in sample i. Note that this term differed from Chen et al. (2019) in that an exact label match was not required.

Separation Loss.

$$\mathcal{L}_{\text{sep}} = \frac{1}{N} \sum_{i=1}^{N} \max_{p \in \mathcal{P}_i^-} S_{ip} \tag{5}$$

This term penalized high similarity between a training sample and prototypes not associated with any of its labels. $\mathcal{P}_i^-$ is the set of prototypes whose class assignments are entirely disjoint from the ground-truth labels of sample i.

Orthogonality Loss.

$$\mathcal{L}_{\text{div}} = \left\| \mathbf{P}\mathbf{P}^\top - \mathbf{I} \right\|_F^2 \tag{6}$$

This discouraged redundancy among prototypes. Let $\mathbf{P} \in \mathbb{R}^{P \times D}$ be the matrix of flattened, row-normalized prototype vectors, and $\mathbf{I}$ the identity matrix. The Frobenius norm measures deviation from orthonormality. This term was directly adapted from Barnett et al. (2024).

Contrastive Loss. Together, our modifications to the clustering and separation loss terms extended their logic from requiring an exact label match between a prototype and a training example, to allowing prototypes to be attracted to any example that contains their assigned class—regardless of what other labels are present. This enabled clustering in the presence of multi-label supervision and implicitly supported overlap among frequently co-occurring diagnoses. However, these terms do not directly structure the relationships between prototypes themselves. To more explicitly shape the geometry of the prototype space based on diagnostic co-occurrence, we introduced a contrastive loss applied at the level of prototype-prototype similarity. This encouraged prototypes assigned to frequently co-occurring classes to remain similar in the latent space, while discouraging similarity between prototypes associated with rarely co-occurring diagnoses.

$$\mathcal{L}_{\text{cntrst}} = -\frac{1}{2}\left(\frac{\sum_{i,j} C_{ij} \cdot \mathrm{S}(p_i, p_j)}{\sum_{i,j} C_{ij}} - \frac{\sum_{i,j} (1 - C_{ij}) \cdot \mathrm{S}(p_i, p_j)}{\sum_{i,j} (1 - C_{ij})} \right) \tag{7}$$

Our contrastive loss was inspired by the Jaccard Similarity Contrastive Loss (JSCL) proposed by Lin et al. (2023) in the context of multi-label text classification. JSCL weights the contrastive objective between sample pairs by the Jaccard similarity of their label sets, allowing for a soft notion of positive and negative pairs in multi-label settings. We adopted this core idea—using Jaccard similarity to scale pairwise contrastive terms—and adapted it to prototype learning by computing similarity between learned prototype vectors. Specifically, we precomputed a Jaccard-based co-occurrence matrix $C \in [0, 1]^{P \times P}$ over the training label set and used it to weight the pairwise similarity score between prototypes.

While our contrastive loss encouraged prototypes of frequently co-occurring classes to remain nearby in the latent space, the model still enforced class-specificity in its decision-making in several ways. First, the classification loss was computed independently for each class using sigmoid activation and binary cross-entropy, ensuring that incorrect predictions were directly penalized regardless of prototype proximity. Second, we included an orthogonality regularization term to promote diversity among prototypes and reduce redundancy. Third, both the branch-specific classifiers and the fusion classifier underwent an L1-constrained convex optimization step after prototype projection, which minimized unnecessary weights and suppressed prototypes that did not meaningfully contribute to final predictions. Together, these mechanisms ensured that similarity in the latent space did not translate into redundant or incorrect activations in the prediction pipeline.

3.5. Training Procedure

Stage 1: Joint Training. We trained each branch independently using the loss defined in Section 3.4. For the final classifier in each branch, we initialized the prototype-to-class

weights $W \in \mathbb{R}^{C \times P}$ such that $W_{cp} = 1$ if prototype p is assigned to class c, and $W_{cp} = -0.5$ otherwise, like the original ProtoPNet (Chen et al., 2019).

Stage 2: Prototype Projection. Each prototype p_j was projected to the latent patch z_i that was most similar (under the similarity metric defined in equation 1), among training samples with label j:

$$p_j^{\text{updated}} = \arg\max_{z_i \in \mathcal{Z}_j} \mathrm{S}(z_i, p_j) \tag{8}$$

where $\mathcal{Z}_j$ denotes the set of all latent patches extracted from training samples that include class j as one of their labels. For *partial prototypes*, z_i represents a local region of the latent space (e.g., a short time window in the morphology branch), and similarity was computed over sliding windows. For *global prototypes*, z_i corresponds to the full latent representation of the input ECG (spanning all timepoints and/or leads). In both cases, the prototype was updated to exactly match the latent patch with the highest similarity among eligible samples.

Stage 3: Fusion Classifier Training. After training and projecting all prototype branches, we froze their weights and extracted the similarity scores for each ECG i. These per-prototype similarity scores from the 1D rhythm, 2D morphology, and 2D global branches were concatenated into a single vector:

$$\mathbf{s}_i = [\mathbf{s}_i^{\text{1D}} \parallel \mathbf{s}_i^{\text{2D-p}} \parallel \mathbf{s}_i^{\text{2D-g}}] \in \mathbb{R}^P \tag{9}$$

where $\mathbf{s}_i \in \mathbb{R}^P$ is the full similarity profile for ECG i and P is the total number of prototypes across all branches. We then trained a fully connected classification layer $W_{\text{fusion}} \in \mathbb{R}^{C \times P}$ on these similarity vectors to predict multi-label diagnoses:

$$\mathcal{L}_{\text{fusion}} = \frac{1}{N} \sum_{i=1}^{N} \mathrm{BCE}(W_{\text{fusion}} \mathbf{s}_i, \mathbf{y}_i) + \lambda \sum_{c=1}^{C} \sum_{j : \mathbf{p}_j \notin \mathcal{P}_c} \left| W_{\text{fusion}}^{(c,j)} \right| \tag{10}$$

This stage used binary cross-entropy loss for multi-label prediction, with L1 regularization to encourage sparsity in the learned fusion weights. The sparsity constraint promoted more selective use of prototype information. Branch-specific classifiers were trained in the same way, to assess if the fusion classifier yielded performance benefits over simple macro-averaging. Additional training and tuning details are provided in Appendices E and F.

3.6. Manual Evaluation of Prototype Quality

To assess the interpretability and perceived clinical utility of the learned prototypes, we conducted a structured review with two practicing physicians. The evaluation focused on the final ProtoECGNet model trained with the full prototype loss suite, including contrastive regularization. Details on the graphical user interface (GUI) used for clinician review and a screenshot of the interface are provided in Appendix C.

The reviewers included a board-certified internist and a board-certified cardiologist. This pairing was selected to reflect both generalist and specialist clinical perspectives. Each reviewer was asked to independently evaluate all available prototypes from the final contrastive model using a lightweight web-based interface. Prototype quality was assessed along two

criteria: 1.) Representativeness. Does the prototype reflect a typical or defining presentation of the assigned diagnostic class? 2.) Clarity. Is the ECG signal in the prototype clean and interpretable, or is it obscured by noise or artifacts that make interpretation difficult?

Each criterion was rated on a 1–5 Likert scale. Reviewers were instructed to score each prototype independently based on the projected ECG segment (see Appendices C and D for additional details). No test cases or model predictions were presented. ECGs that were identified as having label errors by the clinicians were excluded. We report the mean scores and 95% confidence intervals across reviewers for each evaluation criterion.

4. Results & Discussion

We evaluate ProtoECGNet in terms of diagnostic classification performance and prototype interpretability. All results are reported on the held-out PTB-XL test set (fold 10). Macro-AUROC is used as the primary evaluation metric throughout to allow comparison to the PTB-XL benchmarking study (Strodthoff et al., 2021).

4.1. Does explicitly modeling rhythm, morphology, and global abnormalities improve performance over using a single prototype type?

Experiment: To evaluate whether aligning prototype types with clinical reasoning modalities improves performance, we compare models trained on all 71 PTB-XL labels using (1) a single prototype type (e.g., only 1D or 2D CNNs), and (2) the full ProtoECGNet multi-branch model. Each architecture is evaluated as a black-box baseline and as a prototype model with and without contrastive loss. Multi-branch prototype outputs are fused either via simple macro-averaging of branch-specific classifier predictions or a learned fusion classifier on the similarity scores.

Results: The best-performing single-branch model was the 2D partial prototype model with contrastive loss, achieving a macro-AUROC of 0.9137 (See Table 1). However, the full ProtoECGNet model—combining 1D, 2D partial, and 2D global branches—achieved the highest overall performance when using a learned fusion classifier, with a macro-AUROC of 0.9248. This exceeds all single-branch models and closely matches the best-reported performance in the PTB-XL benchmarking study (macro-AUROC 0.925 single-model; 0.929 ensemble) (Strodthoff et al., 2021).

Table 1: Effect of contrastive prototype loss on macro-AUROC across branch-specific, single-branch, and multi-branch settings for ProtoECGNet.

Setting	Model (Label Set)	No Contrastive	w/ Contrastive
Branch-Specific Labels	Rhythm Branch (16 labels)	0.8730	0.8758
	Morphology Branch (52 labels)	0.9023	0.9056
	Global Branch (3 labels)	0.7461	0.8606
Full 71-Label, Single Branch	1D Prototype Model	0.8462	0.8794
	2D Partial Prototype Model	0.9031	0.9137
	2D Global Prototype Model	0.8719	0.8983
Full 71-Label, Multi-Branch	Macro Aggregation	0.8918	0.9048
	Fusion Classifier	0.9010	**0.9248**

Discussion: These results support the hypothesis that modeling distinct diagnostic reasoning types using specialized prototype branches can improve performance. While several single-branch models perform strongly—such as the 2D partial prototype model (0.9137)—they apply a uniform prototype structure to all diagnoses, regardless of their underlying interpretive requirements. In contrast, ProtoECGNet's multi-branch design uses rhythm prototypes for temporal abnormalities, time-localized 2D prototypes for focal morphological findings, and global 2D prototypes for diffuse ECG patterns. The resulting fusion classifier achieves the highest overall macro-AUROC (0.9248), indicating that this domain-tailored architectural structure does not compromise diagnostic performance. Although the performance gains are modest overall, ProtoECGNet matches or exceeds all single-branch models and enables diagnosis-appropriate prototype types that are intended to improve downstream interpretability.

4.2. Does contrastive prototype loss improve diagnostic performance?

Experiment: We evaluate the effect of our proposed contrastive prototype loss across three settings: (1) branch-specific models trained on disjoint label subsets (rhythm, morphology, global), (2) single-branch models trained on all 71 labels, and (3) the full multi-branch model. Each prototype-based model is trained with and without contrastive loss and compared to its corresponding baseline.

Results: Across all settings, contrastive loss improved performance over the standard prototype loss terms (see Table 1). The largest gains were seen in the 2D global branch, where contrastive loss raised macro-AUROC from 0.7461 to 0.8606 in the branch-specific model and from 0.8719 to 0.8983 in the full-label model. Improvements were also observed in the 2D partial model (0.9031 to 0.9137), 1D model (0.8462 to 0.8794), and both multi-branch models. The contrastive loss fusion classifier achieved the highest score (0.9248)

Discussion: These results confirm that contrastive prototype loss consistently enhances diagnostic performance. Improvements were observed across all architectures and label settings, suggesting that our loss formulation provides generalizable gains. This highlights the importance of class co-occurrence-informed regularization in multi-label prototype learning.

4.3. How does ProtoECGNet compare to black-box baselines?

Experiment: For each model variant—1D, 2D partial, 2D global, and multi-branch—we compare a black-box ResNet baseline with the corresponding prototype models (with and without contrastive loss). This allows us to assess whether our interpretable architecture sacrifices diagnostic performance.

Results: Black-box models achieved strong results—0.9219 for the 1D ResNet18 baseline and 0.9060 for 2D ResNet18 (2D Global in Table 2). Prototype-based models trained with contrastive loss approximately matched or surpassed these: the 2D partial model achieved 0.9137 and the 2D global model reached 0.8983. The full ProtoECGNet fusion classifier outperformed all individual black-box models, achieving 0.9248.

Discussion: These results demonstrate that interpretable prototype models can achieve diagnostic performance comparable to traditional black-box CNNs. The 2D partial prototype model surpassed the 2D black-box model, and the final multi-branch model outperformed even the best-performing single-architecture black-box (1D ResNet18). This

Table 2: Macro-AUROC comparison of black-box baselines vs. prototype-based models trained on all 71 labels.

Model Type	Black-Box	Proto (No Contrastive)	Proto (w/ Contrastive)
1D	**0.9219**	0.8462	0.8794
2D Partial	—	0.9031	**0.9137**
2D Global	**0.9060**	0.8719	0.8983
Multi-Branch (Macro Agg.)	0.9052	0.8918	0.9048
Multi-Branch (Fusion Classifier)	—	0.9010	**0.9248**

suggests that prototype-based reasoning, when designed with task-specific structure and contrastive regularization, can achieve state-of-the-art classification while supporting transparent, case-based explanations.

4.4. Are the learned prototypes clinically meaningful?

Experiment: To assess interpretability, we conducted a structured review of all projected prototypes from the final contrastive model. Two physicians—one with board certification in cardiology and one in internal medicine—independently rated each prototype on a 1–5 Likert scale for two criteria: *representativeness* (how well the prototype exemplifies the assigned class) and *clarity* (how visually interpretable and artifact-free the segment is).

Results: Average scores from the clinicians for both criteria are shown in Table 3. In brackets, 95% confidence intervals (CIs) are presented.

Table 3: Average prototype quality scores from structured clinician review (1–5 scale).

Reviewer	Representativeness (95% CI)	Clarity (95% CI)
Cardiologist	4.29 [4.22, 4.35]	4.48 [4.42, 4.54]
Internist	3.59 [3.52, 3.66]	4.73 [4.69, 4.77]

Discussion: These results suggest ProtoECGNet learns meaningful and recognizable ECG patterns which align with clinician expectations. High average scores for both representativeness and clarity indicate that the prototypes are visually interpretable and diagnostically appropriate. This review provides initial validation that the model generates human-interpretable, class-representative prototypes across diverse diagnostic categories but it does not assess downstream utility. Future work plans to include this assessment as a larger user study.

4.5. How does ProtoECGNet support case-based explanations?

Experiment: To evaluate the interpretability of ProtoECGNet's predictions, we qualitatively examined projected prototypes for representative test examples. For each test case, we visualized the most strongly activated prototype and its corresponding training ECG.

Results: We selected one example from each branch—1D rhythm (Figure 3), 2D local morphology (Figure 4), and 2D global (Figure 6).

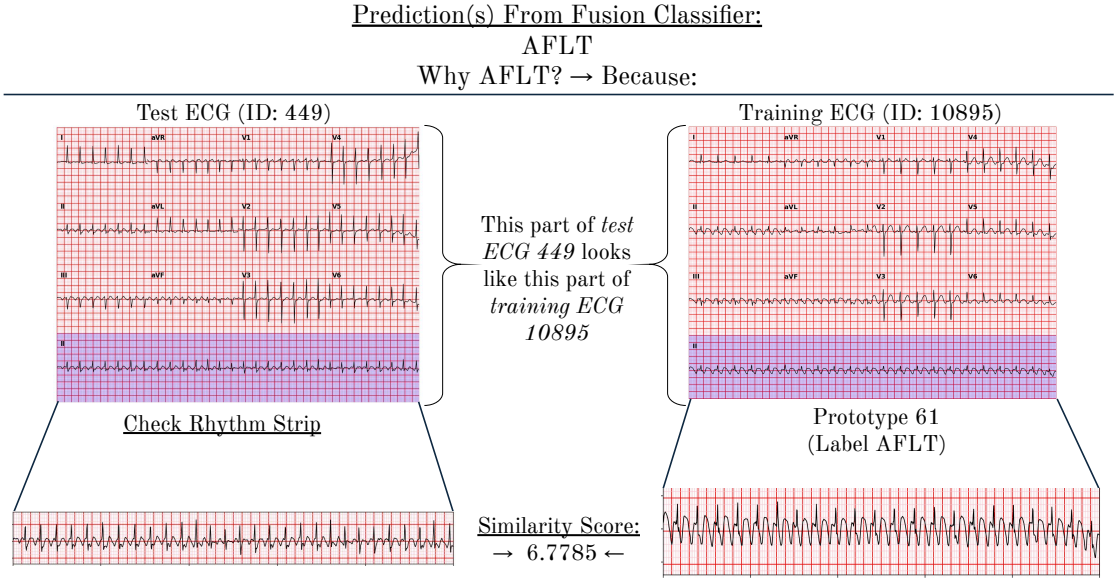

Figure 3: Case-based explanation for atrial flutter (AFLT) predicted by the fusion classifier. The model predicts AFLT for test ECG 449 based on high similarity to prototype 61, which was projected onto training ECG 10895. The top row displays the full 12-lead ECGs for both examples, with rhythm strips (lead II) highlighted in blue to guide interpretation. The bottom row provides a zoomed-in view of these rhythm strips.

Discussion: These qualitative examples illustrate how ProtoECGNet grounds predictions in concrete, case-based reasoning for all three prototype branches. By structuring prototypes to align with rhythm, morphology, and global interpretation styles, the model produces interpretable justifications that mimic clinical reasoning. Unlike saliency maps, these explanations are faithful by design—derived from similarity to real training examples. While this analysis is qualitative, it highlights the explanatory potential of structured prototype learning for real-world decision support.

4.6. Limitations

This study has several limitations that inform directions for future work. First, our prototype taxonomy relies on a manually defined grouping of PTB-XL diagnostic labels into rhythm, morphology, and global categories. While this structure was clinically motivated and grounded in ECG interpretation heuristics, it introduces simplifications that may not fully capture the nuances of certain diagnoses. Some conditions may exhibit features that span multiple reasoning modalities (e.g., both rhythm and morphology), which are not explicitly modeled in the current architecture. Future work could explore more flexible or data-driven grouping strategies.

Second, although our prototype model is designed to support case-based explanation, we did not evaluate its impact on clinical decision-making. Our clinician review focused on

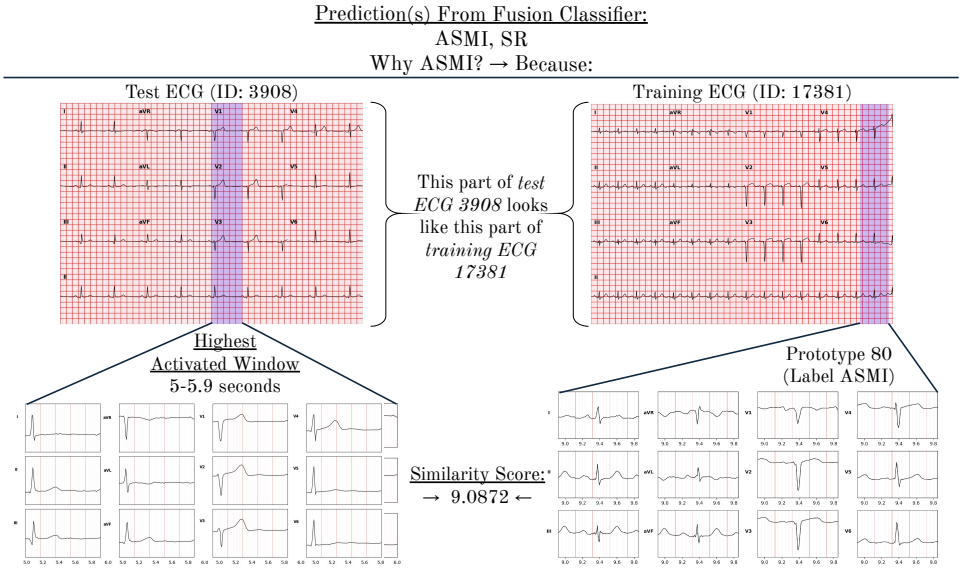

Figure 4: Case-based explanation for anteroseptal myocardial infarction (ASMI) predicted by the fusion classifier. The model predicts ASMI for test ECG 3908, citing strong similarity to prototype 80, which was projected onto a latent patch from training ECG 17381. The top row shows the full 12-lead ECGs for both test and training examples, with the activated region highlighted in blue (5–5.9 seconds for the test ECG and 8.9–9.8 seconds for the prototype). The bottom row zooms into these regions to show all 12 leads. The model appears to have identified a match based on ST-segment elevations in anterior leads (e.g., V2–V4), with a high similarity score of 9.0872.

the clarity and representativeness of projected prototypes, but did not test whether access to these explanations improves trust, diagnostic accuracy, or diagnostic performance. A future blinded user study is needed to quantify how interpretability affects clinical utility.

Third, we used ResNet-based CNNs as the backbone architecture across all experiments to ensure consistency in comparison. While this design choice was appropriate for isolating the effect of prototype modeling and contrastive loss, it may limit performance relative to more recent architectures. ProtoECGNet is modular by design and compatible with alternative backbones, which should be explored to assess potential gains in both accuracy and interpretability.

Finally, our contrastive prototype loss relies on empirical label co-occurrence statistics derived from the PTB-XL training set. These statistics may reflect dataset-specific artifacts or biases and may not generalize across institutions or populations. Methods that learn co-occurrence-aware regularization in a more adaptive or transferable manner remain an area for future work.

5. Conclusions

Our work demonstrated that prototype-based learning can be scaled to complex, multi-label medical time-series tasks like ECG classification without sacrificing performance. By separating diagnostic labels into rhythm, morphology, and global categories, ProtoECGNet enabled the model to learn representations aligned with clinically distinct reasoning processes. Each branch learned prototypes tailored to its diagnostic task, and predictions were grounded in real ECG segments rather than abstract feature maps. Our proposed contrastive loss improved performance by structuring the prototype space to reflect label co-occurrence patterns observed in real-world data. Across all architectures, contrastive training consistently outperformed standard prototype objectives and black-box baselines. Clinician ratings provided an initial indication that the resulting prototypes were clear and representative of their assigned classes. While our evaluation focused on ECGs, the architectural design and contrastive prototype formulation are broadly applicable to other structured time-series tasks in medicine. Future work will explore prospective clinical validation, integration with electronic health records, and expansion to other modalities.

Acknowledgments

This work was funded in part by the National Institutes of Health, specifically grant number R00NS114850 to BKB.

References

Julius Adebayo, Justin Gilmer, Michael Muelly, Ian Goodfellow, Moritz Hardt, and Been Kim. Sanity Checks for Saliency Maps, November 2020. URL http://arxiv.org/abs/1810.03292. arXiv:1810.03292 [cs].

Ravi Aggarwal, Viknesh Sounderajah, Guy Martin, Daniel SW Ting, Alan Karthikesalingam, Dominic King, Hutan Ashrafian, and Ara Darzi. Diagnostic accuracy of deep learning in medical imaging: a systematic review and meta-analysis. *NPJ digital medicine*, 4(1):65, 2021.

David Alvarez-Melis and Tommi S. Jaakkola. Towards Robust Interpretability with Self-Explaining Neural Networks, December 2018. URL http://arxiv.org/abs/1806.07538. arXiv:1806.07538 [cs].

Hayley Barnes, Stephen M Humphries, Peter M George, Deborah Assayag, Ian Glaspole, John A Mackintosh, Tamera J Corte, Marilyn Glassberg, Kerri A Johannson, Lucio Calandriello, et al. Machine learning in radiology: the new frontier in interstitial lung diseases. *The Lancet Digital Health*, 5(1):e41–e50, 2023.

Alina Jade Barnett, Fides Regina Schwartz, Chaofan Tao, Chaofan Chen, Yinhao Ren, Joseph Y. Lo, and Cynthia Rudin. A case-based interpretable deep learning model for classification of mass lesions in digital mammography. *Nature Machine Intelligence*, 3 (12):1061–1070, December 2021. ISSN 2522-5839. doi: 10.1038/s42256-021-00423-x. URL https://www.nature.com/articles/s42256-021-00423-x. Publisher: Nature Publishing Group.

Alina Jade Barnett, Zhicheng Guo, Jin Jing, Wendong Ge, Peter W. Kaplan, Wan Yee Kong, Ioannis Karakis, Aline Herlopian, Lakshman Arcot Jayagopal, Olga Taraschenko, Olga Selioutski, Gamaleldin Osman, Daniel Goldenholz, Cynthia Rudin, and M. Brandon Westover. Improving Clinician Performance in Classifying EEG Patterns on the Ictal–Interictal Injury Continuum Using Interpretable Machine Learning. *NEJM AI*, 1 (6):AIoa2300331, May 2024. doi: 10.1056/AIoa2300331. URL https://ai.nejm.org/doi/full/10.1056/AIoa2300331. Publisher: Massachusetts Medical Society.

Yochai Birnbaum, Kjell Nikus, Paul Kligfield, Miguel Fiol, Jose Antonio Barrabés, Alessandro Sionis, Olle Pahlm, J. Garcia Niebla, and Antonio Bayès de Luna. The Role of the ECG in Diagnosis, Risk Estimation, and Catheterization Laboratory Activation in Patients with Acute Coronary Syndromes: A Consensus Document. *Annals of Noninvasive Electrocardiology : The Official Journal of the International Society for Holter and Noninvasive Electrocardiology, Inc*, 19(5):412–425, September 2014. ISSN 1082-720X. doi: 10.1111/anec.12196. URL https://www.ncbi.nlm.nih.gov/pmc/articles/PMC6932613/.

Mafalda Carrington, Rui Providência, C Anwar A Chahal, Fabrizio Ricci, Andrew E Epstein, Sabina Gallina, Artur Fedorowski, Richard Sutton, and Mohammed Y Khanji. Monitoring and diagnosis of intermittent arrhythmias: evidence-based guidance and role of novel monitoring strategies. *European Heart Journal Open*, 2(6):oeac072, November 2022. ISSN 2752-4191. doi: 10.1093/ehjopen/oeac072. URL https://www.ncbi.nlm.nih.gov/pmc/articles/PMC9683599/.

Chaofan Chen, Oscar Li, Daniel Tao, Alina Barnett, Cynthia Rudin, and Jonathan K Su. This Looks Like That: Deep Learning for Interpretable Image Recognition. In *Advances in Neural Information Processing Systems*, volume 32. Curran Associates, Inc., 2019. URL https://proceedings.neurips.cc/paper_files/paper/2019/hash/adf7ee2dcf142b0e11888e72b43fcb75-Abstract.html.

Ting Chen, Simon Kornblith, Mohammad Norouzi, and Geoffrey Hinton. A Simple Framework for Contrastive Learning of Visual Representations, July 2020. URL http://arxiv.org/abs/2002.05709. arXiv:2002.05709 [cs].

Pierre Elias, Timothy J. Poterucha, Vijay Rajaram, Luca Matos Moller, Victor Rodriguez, Shreyas Bhave, Rebecca T. Hahn, Geoffrey Tison, Sean A. Abreau, Joshua Barrios, Jessica Nicole Torres, J. Weston Hughes, Marco V. Perez, Joshua Finer, Susheel Kodali, Omar Khalique, Nadira Hamid, Allan Schwartz, Shunichi Homma, Deepa Kumaraiah, David J. Cohen, Mathew S. Maurer, Andrew J. Einstein, Tamim Nazif, Martin B. Leon, and Adler J. Perotte. Deep Learning Electrocardiographic Analysis for Detection of Left-Sided Valvular Heart Disease. *JACC*, 80(6):613–626, August 2022. doi: 10.1016/j.jacc.2022.05.029. URL https://www.jacc.org/doi/10.1016/j.jacc.2022.05.029. Publisher: American College of Cardiology Foundation.

Marc Goettling, Alexander Hammer, Hagen Malberg, and Martin Schmidt. xECGArch: a trustworthy deep learning architecture for interpretable ECG analysis considering short-term and long-term features. *Scientific Reports*, 14(1):13122, June 2024. ISSN 2045-2322. doi: 10.1038/s41598-024-63656-x. URL https://www.nature.com/articles/s41598-024-63656-x. Publisher: Nature Publishing Group.

Awni Y. Hannun, Pranav Rajpurkar, Masoumeh Haghpanahi, Geoffrey H. Tison, Codie Bourn, Mintu P. Turakhia, and Andrew Y. Ng. Cardiologist-level arrhythmia detection and classification in ambulatory electrocardiograms using a deep neural network. *Nature Medicine*, 25(1):65–69, January 2019. ISSN 1546-170X. doi: 10.1038/s41591-018-0268-3. URL https://www.nature.com/articles/s41591-018-0268-3. Publisher: Nature Publishing Group.

Peter Hase, Chaofan Chen, Oscar Li, and Cynthia Rudin. Interpretable Image Recognition with Hierarchical Prototypes, August 2019. URL http://arxiv.org/abs/1906.10651. arXiv:1906.10651 [cs].

Bryan He, Alan C Kwan, Jae Hyung Cho, Neal Yuan, Charles Pollick, Takahiro Shiota, Joseph Ebinger, Natalie A Bello, Janet Wei, Kiranbir Josan, et al. Blinded, randomized trial of sonographer versus ai cardiac function assessment. *Nature*, 616(7957):520–524, 2023.

Kaiming He, Xiangyu Zhang, Shaoqing Ren, and Jian Sun. Deep Residual Learning for Image Recognition, December 2015. URL http://arxiv.org/abs/1512.03385. arXiv:1512.03385 [cs].

Rohan Khera, Evangelos K Oikonomou, Girish N Nadkarni, Jessica R Morley, Jenna Wiens, Atul J Butte, and Eric J Topol. Transforming cardiovascular care with artificial intelligence: from discovery to practice: Jacc state-of-the-art review. *Journal of the American College of Cardiology*, 84(1):97–114, 2024.

Prannay Khosla, Piotr Teterwak, Chen Wang, Aaron Sarna, Yonglong Tian, Phillip Isola, Aaron Maschinot, Ce Liu, and Dilip Krishnan. Supervised Contrastive Learning, March 2021. URL http://arxiv.org/abs/2004.11362. arXiv:2004.11362 [cs].

Eunji Kim, Siwon Kim, Minji Seo, and Sungroh Yoon. XProtoNet: Diagnosis in Chest Radiography with Global and Local Explanations, March 2021. URL http://arxiv.org/abs/2103.10663. arXiv:2103.10663 [cs].

Nankai Lin, Guanqiu Qin, Jigang Wang, Aimin Yang, and Dong Zhou. An Effective Deployment of Contrastive Learning in Multi-label Text Classification, July 2023. URL http://arxiv.org/abs/2212.00552. arXiv:2212.00552 [cs].

Chiyu Ma, Brandon Zhao, Chaofan Chen, and Cynthia Rudin. This Looks Like Those: Illuminating Prototypical Concepts Using Multiple Visualizations. *Advances in Neural Information Processing Systems*, 36:39212–39235, December 2023. URL https://proceedings.neurips.cc/paper_files/paper/2023/hash/7b76eea0c3683e440c3d362620f578cd-Abstract-Conference.html.

Yao Ming, Panpan Xu, Huamin Qu, and Liu Ren. Interpretable and Steerable Sequence Learning via Prototypes. In *Proceedings of the 25th ACM SIGKDD International Conference on Knowledge Discovery & Data Mining*, KDD '19, pages 903–913, New York, NY, USA, July 2019. Association for Computing Machinery. ISBN 978-1-4503-6201-6. doi: 10.1145/3292500.3330908. URL https://doi.org/10.1145/3292500.3330908.

Mariana Oliveira, Joana Seringa, Fausto José Pinto, Roberto Henriques, and Teresa Magalhães. Machine learning prediction of mortality in acute myocardial infarction. *BMC Medical Informatics and Decision Making*, 23(1):70, 2023.

David Ouyang, John Theurer, Nathan R Stein, J Weston Hughes, Pierre Elias, Bryan He, Neal Yuan, Grant Duffy, Roopinder K Sandhu, Joseph Ebinger, et al. Electrocardiographic deep learning for predicting post-procedural mortality: a model development and validation study. *The Lancet Digital Health*, 6(1):e70–e78, 2024.

Georgios Petmezas, Leandros Stefanopoulos, Vassilis Kilintzis, Andreas Tzavelis, John A Rogers, Aggelos K Katsaggelos, and Nicos Maglaveras. State-of-the-art deep learning methods on electrocardiogram data: systematic review. *JMIR medical informatics*, 10 (8):e38454, 2022.

Cynthia Rudin. Stop explaining black box machine learning models for high stakes decisions and use interpretable models instead. *Nature Machine Intelligence*, 1(5):206–215, May 2019. ISSN 2522-5839. doi: 10.1038/s42256-019-0048-x. URL https://www.nature.com/articles/s42256-019-0048-x. Publisher: Nature Publishing Group.

Dawid Rymarczyk, Łukasz Struski, Michał Górszczak, Koryna Lewandowska, Jacek Tabor, and Bartosz Zieliński. Interpretable Image Classification with Differentiable Prototypes Assignment. In Shai Avidan, Gabriel Brostow, Moustapha Cissé, Giovanni Maria Farinella, and Tal Hassner, editors, *Computer Vision – ECCV 2022*, pages 351–368, Cham, 2022. Springer Nature Switzerland. ISBN 978-3-031-19775-8. doi: 10.1007/978-3-031-19775-8_21.

Sahil Sethi, Sai Reddy, Mansi Sakarvadia, Jordan Serotte, Darlington Nwaudo, Nicholas Maassen, and Lewis Shi. Toward non-invasive diagnosis of Bankart lesions with deep learning. In *Medical Imaging 2025: Computer-Aided Diagnosis*, volume 13407, pages 854–863. SPIE, April 2025. doi: 10.1117/12.3046251. URL https://www.spiedigitallibrary.org/conference-proceedings-of-spie/13407/134073G/Toward-non-invasive-diagnosis-of-Bankart-lesions-with-deep-learning/10.1117/12.3046251.full.

Nils Strodthoff, Patrick Wagner, Tobias Schaeffter, and Wojciech Samek. Deep Learning for ECG Analysis: Benchmarks and Insights from PTB-XL. *IEEE Journal of Biomedical and Health Informatics*, 25(5):1519–1528, May 2021. ISSN 2168-2208. doi: 10.1109/JBHI.2020.3022989. URL https://ieeexplore.ieee.org/document/9190034. Conference Name: IEEE Journal of Biomedical and Health Informatics.

Rui Sun, Yihao Li, Tianzhu Zhang, Zhendong Mao, Feng Wu, and Yongdong Zhang. Lesion-Aware Transformers for Diabetic Retinopathy Grading. In *2021 IEEE/CVF Conference on Computer Vision and Pattern Recognition (CVPR)*, pages 10933–10942, June 2021. doi: 10.1109/CVPR46437.2021.01079. URL https://ieeexplore.ieee.org/document/9578017. ISSN: 2575-7075.

Sana Tonekaboni, Shalmali Joshi, Melissa D. McCradden, and Anna Goldenberg. What Clinicians Want: Contextualizing Explainable Machine Learning for Clinical End Use.

In *Proceedings of the 4th Machine Learning for Healthcare Conference*, pages 359–380. PMLR, October 2019. URL https://proceedings.mlr.press/v106/tonekaboni19a.html. ISSN: 2640-3498.

Rishi K Trivedi, I-Min Chiu, John Weston Hughes, Albert J Rogers, and David Ouyang. Deep learning on electrocardiogram waveforms to stratify risk of obstructive stable coronary artery disease. *European Heart Journal-Digital Health*, page ztaf020, 2025.

Hugues Turbé, Mina Bjelogrlic, Christian Lovis, and Gianmarco Mengaldo. Evaluation of post-hoc interpretability methods in time-series classification. *Nature Machine Intelligence*, 5(3):250–260, March 2023. ISSN 2522-5839. doi: 10.1038/s42256-023-00620-w. URL https://www.nature.com/articles/s42256-023-00620-w. Publisher: Nature Publishing Group.

Patrick Wagner, Nils Strodthoff, Ralf-Dieter Bousseljot, Dieter Kreiseler, Fatima I. Lunze, Wojciech Samek, and Tobias Schaeffter. PTB-XL, a large publicly available electrocardiography dataset. *Scientific Data*, 7(1):154, May 2020. ISSN 2052-4463. doi: 10.1038/s41597-020-0495-6. URL https://www.nature.com/articles/s41597-020-0495-6. Publisher: Nature Publishing Group.

Jiaqi Wang, Huafeng Liu, Xinyue Wang, and Liping Jing. Interpretable Image Recognition by Constructing Transparent Embedding Space. In *2021 IEEE/CVF International Conference on Computer Vision (ICCV)*, pages 875–884, October 2021. doi: 10.1109/ICCV48922.2021.00093. URL https://ieeexplore.ieee.org/document/9709918. ISSN: 2380-7504.

Yuanyuan Wei, Roger Tam, and Xiaoying Tang. MProtoNet: A Case-Based Interpretable Model for Brain Tumor Classification with 3D Multi-parametric Magnetic Resonance Imaging. April 2023. URL https://openreview.net/forum?id=6Wbj3QCo4U4.

Jia Xie, Zhu Wang, Zhiwen Yu, Yasan Ding, and Bin Guo. Prototype Learning for Medical Time Series Classification via Human–Machine Collaboration. *Sensors*, 24 (8):2655, January 2024. ISSN 1424-8220. doi: 10.3390/s24082655. URL https://www.mdpi.com/1424-8220/24/8/2655. Number: 8 Publisher: Multidisciplinary Digital Publishing Institute.

Neal Yuan, Grant Duffy, Sanket S Dhruva, Adam Oesterle, Cara N Pellegrini, John Theurer, Marzieh Vali, Paul A Heidenreich, Salomeh Keyhani, and David Ouyang. Deep learning of electrocardiograms in sinus rhythm from us veterans to predict atrial fibrillation. *JAMA cardiology*, 8(12):1131–1139, 2023.

Pingyue Zhang and Mengyue Wu. Multi-Label Supervised Contrastive Learning. *Proceedings of the AAAI Conference on Artificial Intelligence*, 38(15):16786–16793, March 2024. ISSN 2374-3468. doi: 10.1609/aaai.v38i15.29619. URL https://ojs.aaai.org/index.php/AAAI/article/view/29619. Number: 15.

Jianwei Zheng, Jianming Zhang, Sidy Danioko, Hai Yao, Hangyuan Guo, and Cyril Rakovski. A 12-lead electrocardiogram database for arrhythmia research covering

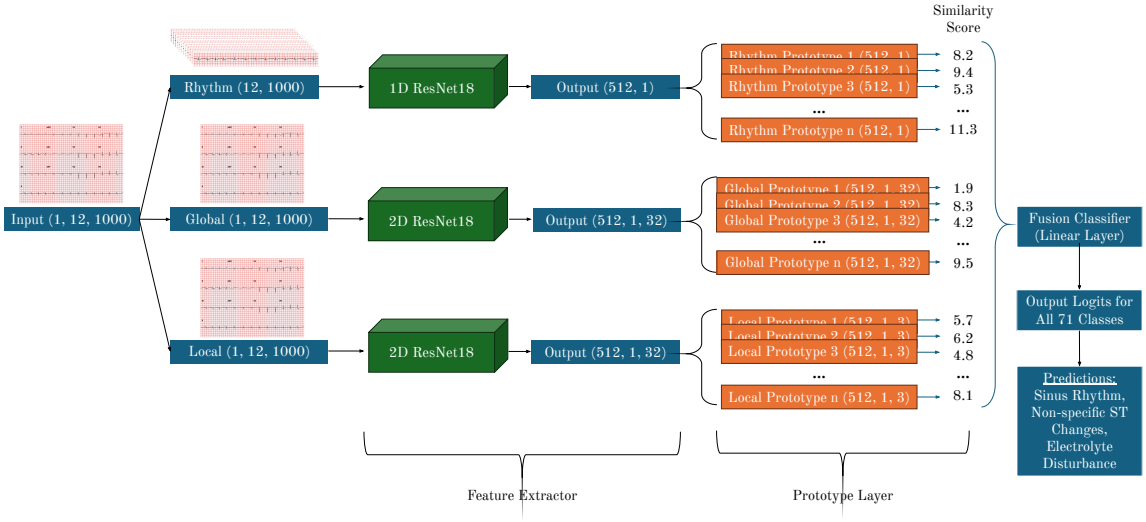

Figure 5: Internal ProtoECGNet architecture. Each input ECG is simultaneously passed through three branches corresponding to distinct clinical reasoning types: (1) a 1D CNN with global temporal prototypes for rhythm interpretation, (2) a 2D CNN with time-localized prototypes for morphological patterns across leads, and (3) a 2D CNN with global prototypes for diffuse signal abnormalities. Each branch is trained independently on its assigned diagnostic label subset, and outputs a similarity score for each class. A linear layer is then trained to map these similarity scores to class logits.

more than 10,000 patients. *Scientific Data*, 7(1):48, February 2020. ISSN 2052-4463. doi: 10.1038/s41597-020-0386-x. URL https://www.nature.com/articles/s41597-020-0386-x. Publisher: Nature Publishing Group.

Appendix A. ProtoECGNet Internal Architecture

Figure 5 contains a detailed overview of the internal architecture of each branch of ProtoECGNet.

Appendix B. Example of a Case-Based Explanation from the 2D Global Branch

Figure 6 contains a case-based explanation for a diagnosis processed via the 2D global branch of ProtoECGNet.

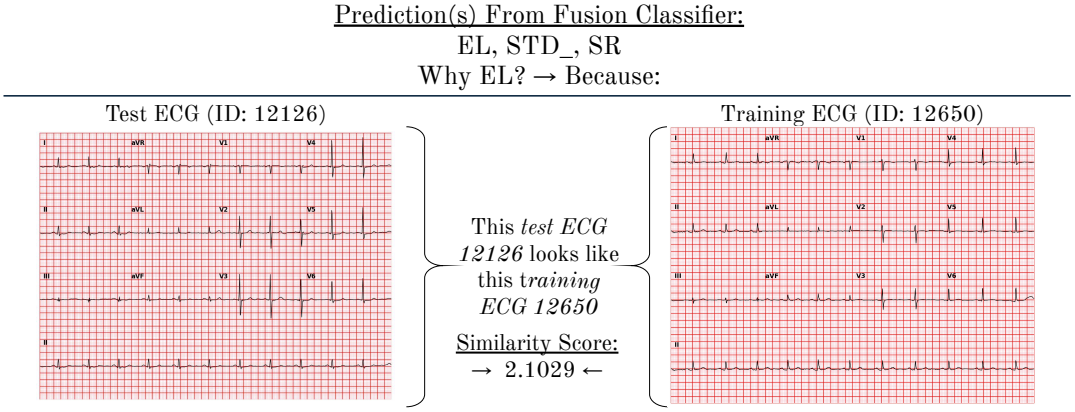

Figure 6: Case-based explanation for an electrolyte disturbance (EL) predicted by the fusion classifier. The model predicts EL for test ECG 12126, citing strong similarity to an EL prototype that was projected onto training ECG 12650. Since this diagnosis uses 2D global prototypes, full 12-lead ECGs are shown for both the test and training examples—along with their similarity score.

Appendix C. Prototype Review Interface

We developed a lightweight web interface to display projected prototypes for clinician evaluation. Each prototype was rendered as a traditional 12-lead ECG with a red grid and standard calibration, labeled only by its diagnostic class. Reviewers scored each prototype independently across multiple dimensions using dropdown menus and selection boxes. A screenshot of the interface is shown in Figure 7.

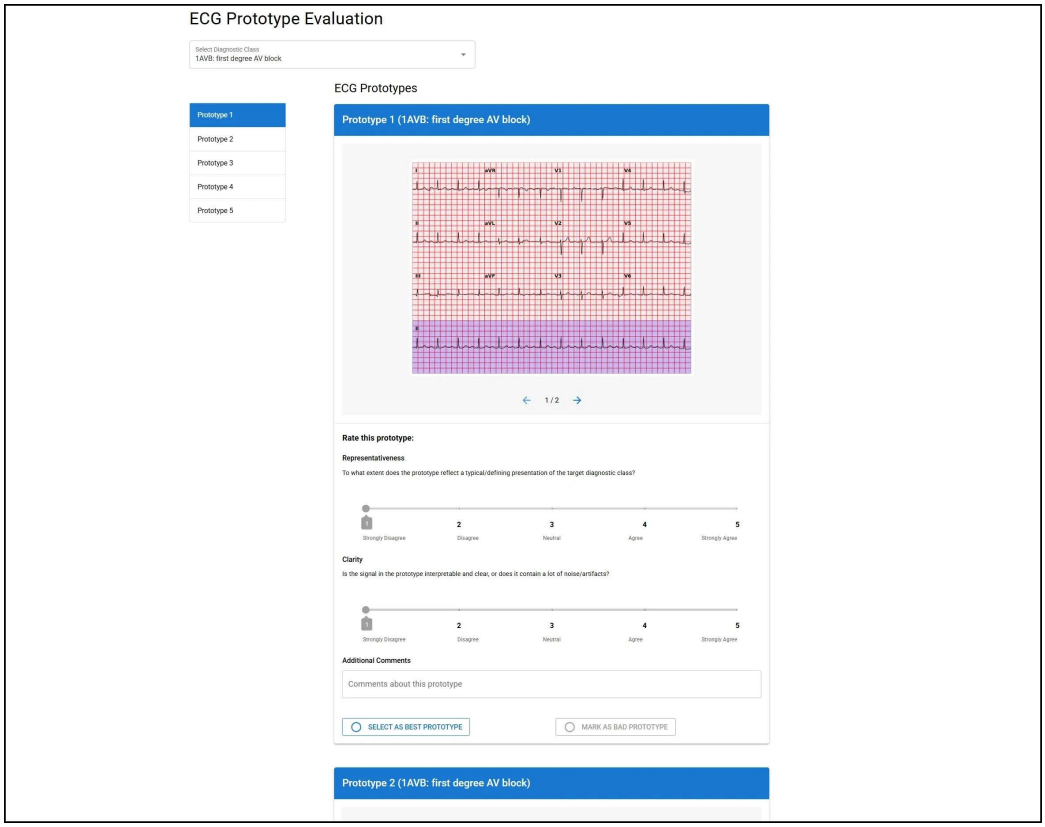

Figure 7: Clinician review interface for prototype evaluation.

Appendix D. ECG and Prototype Visualization

All ECG visualizations follow the conventional clinical 12-lead layout. The top three rows display 2.5-second segments from leads I, II, III → aVR, aVL, aVF → V1–V6 in standard order, and the bottom row shows a continuous 10-second rhythm strip from lead II. This format is widely used in clinical ECG interpretation and was applied consistently in both the clinician review interface and all prototype figures to ensure familiarity for clinicians.

For each prototype, we visualize the training ECG segment that produced the latent patch onto which the prototype was projected. All branches of the model—including the 1D rhythm branch—receive the full 10-second, 12-lead ECG as input. For global prototypes (used in the 1D rhythm and 2D global branches), we display the full ECG. In the 1D rhythm branch, as the model does not explicitly model inter-lead spatial relationships, we highlight the bottom rhythm strip (lead II) to help viewers interpret the temporal pattern recognized by the model. For partial prototypes (2D morphology branch), we highlight the exact 0.94-second window (3 of 32 latent time steps) that was selected during prototype projection. To reflect the fact that the model considers all 12 leads within this window, we also include a full-lead cutout of the selected time segment, allowing assessment of local inter-lead waveform morphology. These visualizations provide clinically grounded and semantically faithful views of the prototype segments used by the model to support its predictions.

Appendix E. Implementation Details

All models were implemented in PyTorch. We used the Adam optimizer, and explored cosine annealing, cyclic, and step-based learning rate schedulers during hyperparameter tuning. Each model was trained for up to 200 epochs, with early stopping applied if validation macro-AUROC did not improve for 10 consecutive epochs. Model checkpoints were saved based on the best validation AUROC, and the corresponding weights were used for inference and testing.

Hyperparameter tuning was conducted using Optuna with 200 trials per model variant. Tuned parameters included learning rate, weight decay, dropout rate, and learning rate scheduler configuration. Both the joint training phase and the classifier stage (including the fusion classifier and branch-specific classifiers) were tuned independently using this strategy. Loss weightings for each prototype loss term ($\lambda_{\text{clst}}, \lambda_{\text{sep}}, \lambda_{\text{div}}, \lambda_{\text{cntrst}}$) were also included as tunable parameters.

When contrastive loss was not used, we adopted the prototype loss coefficients from Barnett et al. (2024). For contrastive models, we conducted a dedicated 1000-trial Optuna sweep to tune all four loss coefficients. This sweep fixed non-loss hyperparameters (dropout = 0.3, batch size = 32, learning rate = 0.001, scheduler = ReduceLROnPlateau, L2 weight decay = 1×10^{-4}), and only optimized the four loss weights. This was run separately for the 1D rhythm, 2D partial, and 2D global prototype branches; the resulting optimal values were relatively consistent across branches, and we selected rounded values that fell between the final tuned values of all three branches. These values were then held fixed in all subsequent experiments using contrastive regularization.

Prototype-based models underwent a three-stage training procedure (Section 3.5). Stage 1 (joint training) and Stage 2 (prototype projection) were repeated once to allow the prototypes to better converge on class-representative features, after which performance typically stabilized (no further increases in validation AUC). Stage 3 (fusion classifier training) was conducted only once, after freezing the prototype branches.

Appendix F. System Requirements

All model training and inference were conducted on a high-performance computing cluster using a single NVIDIA A100 GPU with 40GB memory. Models were implemented in Python 3.10 using PyTorch 2.6.0 and PyTorch Lightning 2.5.0. Training visualization was performed with TensorBoard, and ECG data handling used Pandas and WFDB. Hyperparameter optimization was conducted with Optuna 4.2.1. All code was executed in a SLURM-managed Linux environment with CUDA 12 and cuDNN 9.1.

Appendix G. Diagnostic Groupings

Each of the 71 PTB-XL diagnostic labels was assigned to one of three prototype branches based on the type of visual reasoning required for diagnosis. These groupings were defined by two board-certified physicians (one cardiologist & one internist) and used to train the corresponding branch of ProtoECGNet. The full list of SCP codes and their assigned groupings is shown below.

1D Rhythm Branch (16 diagnoses)

- 1AVB: first degree AV block
- 2AVB: second degree AV block
- 3AVB: third degree AV block
- AFIB: atrial fibrillation
- AFLT: atrial flutter
- BIGU: bigeminal pattern (unknown origin, SV or ventricular)
- IVCD: nonspecific intraventricular conduction disturbance
- PACE: artificial pacemaker
- PSVT: paroxysmal supraventricular tachycardia
- SARRH: sinus arrhythmia
- SBRAD: sinus bradycardia
- SR: sinus rhythm
- STACH: sinus tachycardia
- SVARR: supraventricular arrhythmia
- SVTAC: supraventricular tachycardia
- TRIGU: trigeminal pattern (unknown origin, SV or ventricular)

2D Morphology Branch (52 diagnoses)

- ABQRS: abnormal QRS
- ALMI: anterolateral myocardial infarction
- AMI: anterior myocardial infarction
- ANEUR: ST-T changes from ventricular aneurysm
- ASMI: anteroseptal myocardial infarction
- CLBBB: complete left bundle branch block
- CRBBB: complete right bundle branch block
- HVOLT: high QRS voltage
- ILBBB: incomplete left bundle branch block
- ILMI: inferolateral myocardial infarction

- IMI: inferior myocardial infarction
- INJAL: injury in anterolateral leads
- INJAS: injury in anteroseptal leads
- INJIL: injury in inferolateral leads
- INJIN: injury in inferior leads
- INJLA: injury in lateral leads
- INVT: inverted T waves
- IPLMI: inferoposterolateral myocardial infarction
- IPMI: inferoposterior myocardial infarction
- IRBBB: incomplete right bundle branch block
- ISCAL: ischemia in anterolateral leads
- ISCAN: ischemia in anterior leads
- ISCAS: ischemia in anteroseptal leads
- ISCIL: ischemia in inferolateral leads
- ISCIN: ischemia in inferior leads
- ISCLA: ischemia in lateral leads
- ISC_: nonspecific ischemia
- LAFB: left anterior fascicular block
- LAO/LAE: left atrial overload/enlargement
- LMI: lateral myocardial infarction
- LNGQT: long QT interval
- LOWT: low amplitude T waves
- LPFB: left posterior fascicular block
- LPR: prolonged PR interval
- LVH: left ventricular hypertrophy
- LVOLT: low QRS voltage
- NDT: nondiagnostic T abnormalities
- NST_: nonspecific ST changes

- NT_: nonspecific T wave changes
- PAC: premature atrial complex
- PMI: posterior myocardial infarction
- PRC(S): premature complexes
- PVC: premature ventricular complex
- QWAVE: Q waves present
- RAO/RAE: right atrial overload/enlargement
- RVH: right ventricular hypertrophy
- SEHYP: septal hypertrophy
- STD_: ST depression
- STE_: ST elevation
- TAB_: T wave abnormality
- VCLVH: voltage criteria for LVH
- WPW: Wolff-Parkinson-White syndrome

2D Global Branch (3 diagnoses)

- DIG: digitalis effect
- EL: electrolyte disturbance or drug effect
- NORM: normal ECG